*Nano Research* 2017, 10(9): 2923–2933
DOI 10.1007/s12274-017-1502-x
**Research Article**
ISSN 1998-0124
CN 11-5974/O4

# Sandwich-structured nanocomposites of N-doped graphene and nearly monodisperse $Fe_3O_4$ nanoparticles as high-performance Li-ion battery anodes

Wen Qi[1], Xuan Li[2], Hui Li[3], Weikang Wu[3], Pei Li[2], Ying Wu[1], Chunjiang Kuang[1], Shaoxiong Zhou[1] (✉), and Xiaolin Li[4] (✉)

[1] *Beijing Key Laboratory of Energy Nanomaterials, Advance Technology & Materials Co., Ltd., China Iron & Steel Research Institute Group, Beijing 100081, China*
[2] *School of Materials Science and Engineering, Tianjin University, Tianjin 300072, China*
[3] *Key Laboratory for Liquid–Solid Structural Evolution and Processing of Materials, Ministry of Education, Shandong University, Jinan 250061, China*
[4] *Department of Stationary Energy Storage, Pacific Northwest National Laboratory, Richland, Washington 99354, USA*

**Received:** 11 October 2016
**Revised:** 12 January 2017
**Accepted:** 31 January 2017



## KEYWORDS

N-doped graphene,
iron oxides,
self-assembly,
Li-ion battery,
density functional theory

## ABSTRACT

Iron oxides have attracted considerable interest as abundant materials for high-capacity Li-ion battery anodes. However, their fast capacity fading owing to poorly controlled reversibility of the conversion reactions greatly hinders their application. Here, a sandwich-structured nanocomposite of N-doped graphene and nearly monodisperse $Fe_3O_4$ nanoparticles were developed as high-performance Li-ion battery anode. N-doped graphene serves as a conducting framework for the self-assembled structure and controls $Fe_3O_4$ nucleation through the interaction of N dopants, surfactant molecules, and iron precursors. $Fe_3O_4$ nanoparticles were well dispersed with a uniform diameter of ~15 nm. The unique sandwich structure enables good electron conductivity and Li-ion accessibility and accommodates a large volume change. Hence, it delivers good cycling reversibility and rate performance with a capacity of ~1,227 $mA{\cdot}h{\cdot}g^{-1}$ and 96.8% capacity retention over 1,000 cycles at a current density of 3 $A{\cdot}g^{-1}$. Our work provides an ideal structure design for conversion anodes or other electrode materials requiring a large volume change.

## 1 Introduction

Because of their high energy density and long cycle life, Li-ion batteries (LIBs) are excellent for powering portable electronics and electric vehicles. In order to meet the demand for LIBs with a higher energy and a lower cost, fabricating high-capacity electrodes from nontoxic, inexpensive, and abundant materials is

Address correspondence to Shaoxiong Zhou, sxzhou@atmcn.com; Xiaolin Li, xiaolin.Li@pnnl.gov

essential. Transition metal oxides based on conversion reactions can be reduced to form metal nanoclusters and $Li_2O$, resulting in a significantly higher capacity than that of the graphite electrode (~372 mA·h·g$^{-1}$) used in state-of-the-art LIBs [1–4]. However, it also leads to a large volume change and can destroy the structure upon electrochemical cycling. The capacity of metal oxide electrodes usually fades quickly because the conversion reaction has poor reversibility, especially at high rates [5, 6].

Metal oxide nanoparticles and nanostructures have been used in composites with conductive carbon [7–9], carbon nanotubes [10–13], hollow/mesoporous structures [14–16], or graphene [17–22] to improve their reversibility and cycling stability. For example, binder-free $Fe_3O_4$/single-wall nanotube hybrid electrodes delivered a capacity of ~850 mA·h·g$^{-1}$ at a 5 C rate [10]. The capacity retention was ~80% over 100 cycles. A multifunctional ternary heterostructure of $TiO_2$/$Fe_3O_4$/graphene developed recently showed stability over 160 cycles with at initial capacity of ~400 mA·h·g$^{-1}$ at a current density of ~1 A·g$^{-1}$ [23]. Nanoparticles have been anchored on graphene as a substrate to prevent the aggregation and pulverization of nanoparticles upon cycling [23–28]. For example, $SnO_2$ nanocrystals were deposited on graphene sheets and formed layered structures, which greatly improved the cycling stability [29]. We have also demonstrated that graphene can serve as a molecular template to control the nucleation and self-assembly of the composite structure by tuning the functional group/defect density [30]. Recently, nitrogen-doped graphene sheets (N-GS) have emerged as a promising supporting matrix to improve the cycling stability and rate performance of LIBs, Li-S batteries, etc. [31–35]. Doping N heteroatoms into the graphene lattice is believed to tune the electronic features, leading to stronger molecular adsorption and interfacial binding [24, 36–38] and hence greatly improving the electrochemical performance [39–44]. $Fe_3O_4$ is a nontoxic, abundant, and environmentally benign material. It has a high theoretical capacity of ~928 mA·h·g$^{-1}$ and is thus considered one of the most promising conversion electrode materials [45–49]. Recently, various graphene–$Fe_3O_4$ composites have been developed to address the poor cycle life of $Fe_3O_4$. For example, three-dimensional N-GS/$Fe_3O_4$ prepared by a hydrothermal method exhibited a high reversible capacity and good cycling stability at a low current density of 100 mA·g$^{-1}$. The capacity is ~1,130 mA·h·g$^{-1}$ after 200 cycles [41]. A $Fe_3O_4$ nanoparticle electrode encapsulated in N-GS [50] delivered a capacity of up to 800 mA·h·g$^{-1}$ after 100 cycles at a current density of 100 mA·g$^{-1}$. However, achieving high-rate $Fe_3O_4$ electrodes with long-term cycling stability remains a significant challenge.

Here, we developed a self-assembly process to synthesize sandwich-structured nanocomposites of N-GS and $Fe_3O_4$ nanoparticles. The N-GS not only works as the conducting framework but also controls the iron oxide nucleation through the strong interaction between N atoms in the graphene planes, surfactant molecules, and iron precursors. The $Fe_3O_4$ nanoparticles have a nearly monodisperse diameter of ~15 nm and nucleate favorably on N-GS around N sites. The dopant-controlled nucleation process was elucidated with a combined theoretical and experimental study. The uniquely structured nanocomposite promises to deliver good cycling reversibility and rate performance because of its good conductivity, Li-ion accessibility, and ability to accommodate a volume change. A capacity of ~1,227 mA·h·g$^{-1}$ with 96.8% retention over 1,000 cycles was demonstrated at the current density of 3 A·g$^{-1}$.

## 2 Results and discussion

The sandwich-structured nanocomposite of N-GS/$Fe_3O_4$ was obtained by a self-assembly process in a one-step hydrothermal reaction. The schematic in Fig. 1(a) elucidates the formation process: 1) Functionalized graphene sheets (FGS) or graphene oxide (GO) as molecular templates self-assembled with surfactant molecules and iron precursor/iron oxide clusters. Surfactants and iron precursor/iron oxide clusters form hemi-micelles on GO when the surfactant concentration is higher than the critical micelle concentration (CMC) [30]. 2) GO was reduced by hydrazine to form graphene sheets, thereby doping the graphene with nitrogen [3]. 3) The iron precursors hydrolyzed, nucleated on N-GS, and grew into $Fe_3O_4$ nanoparticles [3, 30]. Usually, functional groups/defects on GO/FGS

control the nucleation [30]. In the case of the N-GS/$Fe_3O_4$ composite, $Fe_3O_4$ nanoparticles mostly anchored around the N sites because other functional groups were reduced/removed during the hydrothermal treatment. The experimental results and simulation data (vide infra) revealed further details of the N-GS-controlled nucleation. 4) After the loss of the charges and functional groups from the GO, N-GS restacked on each other, forming a sandwich-structured nanocomposite.

The morphology and structure of the obtained N-GS/$Fe_3O_4$ were investigated using scanning electron microscopy (SEM) and transmission electron microscopy (TEM). As shown in Figs. 1(b)–1(d) and Fig. S1 (in the Electronic Supplementary Material (ESM)), the surfactant amount greatly affected the $Fe_3O_4$ particle size and dispersion. With the appropriate amount of hexadecyltrimethylammonium bromide (CTAB) (~0.3 g), $Fe_3O_4$ nanoparticles were well dispersed on

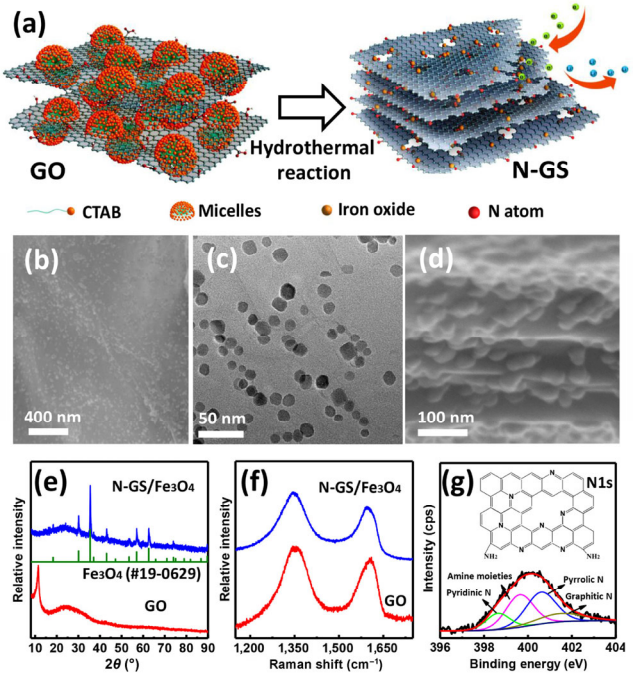


**Figure 1** (a) Schematic illustration of the self-assembly process of surfactants, N-GS, and $Fe_3O_4$; (b) SEM image of N-GS/$Fe_3O_4$-0.3 showing the surface morphology; (c) typical TEM image of N-GS/$Fe_3O_4$-0.3; (d) SEM image of the cross-section of N-GS/$Fe_3O_4$-0.3 showing the sandwich structure; (e) XRD patterns of GO and N-GS/$Fe_3O_4$-0.3; (f) Raman spectra of GO and N-GS/$Fe_3O_4$-0.3; (g) high-resolution XPS N1s spectrum of N-GS/$Fe_3O_4$-0.3. Inset are the different configurations of nitrogen atoms in N-doped graphene.

the N-GS plane with a nearly monodisperse diameter of ~15 nm (Figs. 1(b) and 1(c)). No free $Fe_3O_4$ nanoparticles were observed outside of N-GS, indicating strong binding between the $Fe_3O_4$ nanoparticles and N-GS. Large agglomerates of $Fe_3O_4$ were obtained when there was either not enough or too much CTAB (Fig. S1 in the ESM). The particle size and distribution of $Fe_3O_4$ greatly affected the electrochemical reversibility and battery performance. The correlation of the CTAB amount with the $Fe_3O_4$ structure and the electrodes' electrochemical performance will be discussed later.

Figure 1(d) shows a cross-sectional SEM image of N-GS/$Fe_3O_4$-0.3 (the samples are denoted according to the CTAB amount. See experimental section for details.). It exhibits an ordered sandwich structure with $Fe_3O_4$ nanoparticles loaded between the graphene layers. The sandwich structure exhibits the following advantages for battery applications: 1) It provides enough void space to accommodate the volume change from the conversion reaction. 2) It also provides $Li^+$ ions in the electrolyte good accessibility to the electrode surface, both of which are important in enabling good cycling stability and rate performance (vide infra). 3) The re-stacking of graphene sheets helps to improve the composite packing density, which imparts a higher battery energy density than that of porous structures. The Brunauer–Emmett–Teller (BET) surface area of N-GS/$Fe_3O_4$-0.3 (Fig. S2 in the ESM) is ~40 $m^2 \cdot g^{-1}$, much lower than that of the porous materials reported in the literature [51, 52].

X-ray diffraction (XRD), Raman and X-ray photoelectron spectroscopy (XPS) show the reduction of graphene oxide and N-doping. Figure 1(e) shows the XRD patterns of GO and N-GS/$Fe_3O_4$-0.3. The XRD pattern of GO (red curve) has a characteristic (002) diffraction peak at $2\theta = 11°$ with a larger basal spacing of 0.90 nm, consistent with Ref. [53]. The XRD pattern of N-GS/$Fe_3O_4$-0.3 nanocomposites (blue line) shows strong peaks from the magnetite $Fe_3O_4$ (JCPDS card 19-0629). The diffraction peak of GO at 11° disappeared, and no graphite peak was observed. This indicates that the formation of $Fe_3O_4$ particles mitigated graphene re-stacking [14, 54].

The Raman spectra of GO and N-GS/$Fe_3O_4$-0.3 reveal the structural change from GO to graphene (Fig. 1(f)). GO (red curve) exhibits a strong D band at ~1,346 $cm^{-1}$

(originating from defects associated with vacancies, grain boundaries, and amorphous carbon species) and a G band at ~1,601 $cm^{-1}$ (corresponding to ordered $sp^2$-bonded carbon atoms). The D/G ratio ($I_D/I_G$) is ~1.12. The Raman spectrum of N-GS/$Fe_3O_4$-0.3 also shows D and G bands, but the G band shifts to a lower wavenumber of ~1,596 $cm^{-1}$, indicating the reduction of GO [54]. The D/G ratio remained similar at ~1.26, indicating the average size of the $sp^2$ domains remained after the reduction of GO and nitrogen doping [41]. This is believed to be the reason for the good conductivity and improved electrochemical performance.

XPS results for GO, N-GS, and N-GS/$Fe_3O_4$ corroborate the GO reduction and the doping of nitrogen. The GO reduction is confirmed by the decrease in the oxygen amount in the N-GS sample without $Fe_3O_4$ (Figs. S3(a)–S3(c) in the ESM). The oxygen percentage of GO is 36.09 at.%, which is much higher than that of the control N-GS sample without $Fe_3O_4$ (10.1 at.%), thus indicating the functional groups of GO were successfully removed after the hydrothermal reaction. Figures S3(d) and S3(e) in the ESM, and Fig. 1(g) are the XPS survey scan and the high-resolution C1s and N1s spectra of N-GS/$Fe_3O_4$-0.3. The nitrogen percentage is ~3.34 at.%, and it is incorporated in multiple chemical states [55, 56]. The high-resolution N1s spectra (Fig. 1(g)) could be fitted into four peaks at 398.9, 399.6, 400.6, and 401.5 eV corresponding to pyridinic N, amine moieties or other $sp^3$-C/N bonds, pyrrolic N and graphitic N, respectively. A small C=N signal at 285.8 eV is observed in the C1s XPS of N-GS/$Fe_3O_4$-0.3 (Fig. S3(e) in the ESM), which also showed a stronger C=C peak at 284.5 eV than the C1s XPS of GO (Fig. S3(b) in the ESM). This further demonstrates the de-oxygenation as well as nitrogen incorporation during the hydrothermal process. XPS also confirms the formation of $Fe_3O_4$. The high-resolution Fe2p spectrum (Fig. S3(f) in the ESM) shows two peaks around 711.2 and 724.5 eV and no satellite peak around 719.2 eV. This is consistent with the results for $Fe_3O_4$ in the Refs. [18, 57], further corroborating the XRD results.

High-resolution TEM (HRTEM) and energy-dispersive X-ray spectroscopy (EDS) mapping were used to further study the structure of N-GS/$Fe_3O_4$-0.3. Figure 2(a) shows a typical HRTEM image of several $Fe_3O_4$ nanoparticles on N-GS. The particles are ~15 nm in diameter. The lattice fringes with basal distances were ~0.25 nm, corresponding to the (311) lattice spacing of magnetite $Fe_3O_4$ phase (JCPDS card 19-0629).

Figures 2(b)–2(f) are TEM image and the corresponding EDS mapping of C, N, Fe, and O, respectively, which reveal the element distributions and the correlation between N-doping and $Fe_3O_4$ nucleation. Figure 2(c) shows the C distribution, which resembles the shape of the graphene sheet in Fig. 2(b). Nitrogen also covers almost every part of the graphene sheet but exhibits slightly stronger signals in certain areas (Fig. 2(d)). Closer inspection reveals that the pattern of the areas with condensed N signal (areas marked with white circles in Fig. 2(d)) overlaps very well with the Fe (Fig. 2(e)) and oxygen map (Fig. 2(f)). This corroborates the points 3) and 4) in the earlier discussion of the self-assembly process (schematically shown in Fig. 1(a)) and is consistent with our previous finding that the functional groups/defects control the nucleation [30]. Most other functional groups on GO were reduced/removed during the hydrothermal process, and hence, $Fe_3O_4$ primarily nucleated at the highly N-doped sites. The oxygen map resembles the Fe map because the majority of oxygen signal is from $Fe_3O_4$.

To understand the preferential bonding between $Fe_3O_4$ and N-GS, density functional theory (DFT) calculations were used to simulate the electron density (Fig. 3) and absorption energy (Table S1 in the ESM)

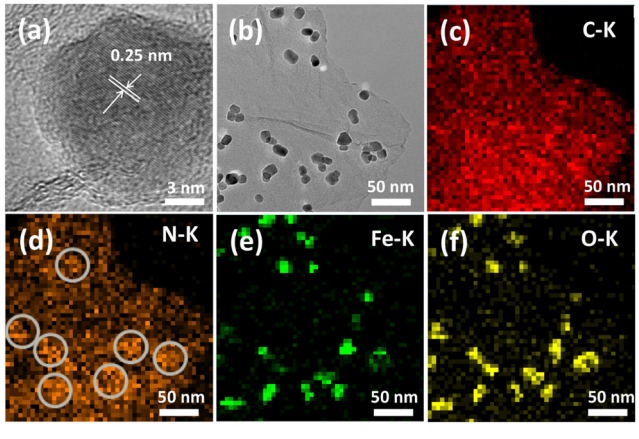


**Figure 2** (a) HRTEM image of N-GS/$Fe_3O_4$-0.3, (b)–(f) TEM image and corresponding mapping images of C, N, Fe, and O.

of different graphene substrates with $Fe_3O_4$ clusters. Figure 3 shows the electron density of perfect graphene (Fig. 3(a), denoted as PG), graphene with graphitic N (Fig. 3(b), denoted as NG) and graphene with pyridinic N (Fig. 3(c), denoted as NVG) (see details in the ESM). The electron density of the substrates illustrates the probability of an electron being present at a specific location, indicating the potential to adsorb $Fe_3O_4$ clusters. The different colors, from blue to red in the graphical images of electron density, are labeled in terms of the percentage of total electrons enclosed. The red region has the most electrons, followed by the yellow region, while the electron density in the blue region is quite low. Figure 3 shows more red (i.e., the most electrons) near N atoms on NG and NVG substrates, indicating the stronger electronegativity of N atoms. This could facilitate the adsorption of $Fe_3O_4$ clusters onto the nitrogen-doped graphene surface. The chemical potentials ($\mu_{Fe_3O_4}$) of adsorbed $Fe_3O_4$ clusters on the three substrates mentioned above (see right column of Fig. 3) were further determined using periodic DFT calculations, and the results are given

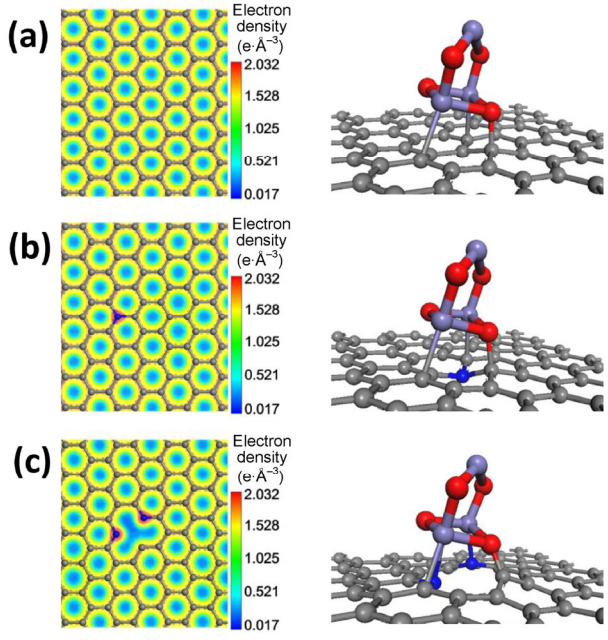


**Figure 3** DFT results of the electron density distribution map and optimized structures of $Fe_3O_4$ clusters on (a) perfect graphene, (b) N-doped graphene with graphitic N, and (c) N-doped vacancy graphene with pyridinic N. The left column shows the electron density distribution map. The right columns are the side views of $Fe_3O_4$ clusters on different graphene substrates.

in Table S1 (in the ESM). The $\mu_{Fe_3O_4}$ of $Fe_3O_4$ clusters on the NVG is –20.48 eV, which is much lower than that on PG and NG, indicating the enhanced stabilization and bonding of $Fe_3O_4$ on N-doped graphene sheets. The $\mu_{Fe_3O_4}$ of $Fe_3O_4$ clusters on the NG shows similar absorption energy to that of pristine graphene. Thus, it is safe to conclude that the DFT calculation results clearly elucidated the overlapping of N and Fe elements. The strong interaction between $Fe_3O_4$ and N-doped graphene results in a more uniform particle dispersion. Together with the advantages of the unique sandwich structure and the nearly monodisperse nanoparticle size, this nanocomposite promises to deliver good cycling and rate performance.

The cyclic voltammetry (CV) measurements and battery tests (Fig. 4) confirm good electrochemical performance and reversibility of the conversion reaction. The CV of N-GS/$Fe_3O_4$-0.3 was obtained at 0.01 mV·s$^{-1}$ between 0.01 and 3.0 V (Fig. 4(a)). A clear, sharp cathodic peak at 0.62 V was observed during the first lithiation step. This corresponds to the conversion process of $Fe_3O_4$ to Fe and the formation of amorphous $Li_2O$ as well as side reactions of the electrolyte decomposition [58]. The cathodic peak at ~0 V is attributed to the reaction of lithium ions with the N-GS, consistent with the CV of the control N-GS sample (Fig. S4 in the ESM). Two anodic peaks are observed at 1.61 and 1.83 V, which can be ascribed to the reversible oxidation of $Fe^0$ to $Fe^{2+}$/$Fe^{3+}$. In the second cycle, the two main cathodic peaks shift to 0.8 and 1.2 V due to polarization and the structural change in the $Fe_3O_4$ nanoparticles after Li-ion insertion during the first cycle [58]. In subsequent cycles, both the peak current and the integral area nearly overlapped with each other, demonstrating good reversibility. The CV of the control N-GS sample (Fig. S4 in the ESM) has a cathodic peak at 0.6 V and a sharp peak at ~0 V in the first cycle. The peak at 0.6 V completely disappeared in the following cycles, indicating irreversible reactions associated with electrolyte decomposition. The sharp cathodic peak at ~0 V originated from the lithiation of N-GS.

Figure 4(b) shows selected charge/discharge curves (the 1st, 50th, and 150th cycles) of a typical N-GS/$Fe_3O_4$-0.3 electrode. Similar voltage profiles are observed, yet the plateaus shortened and the polarization

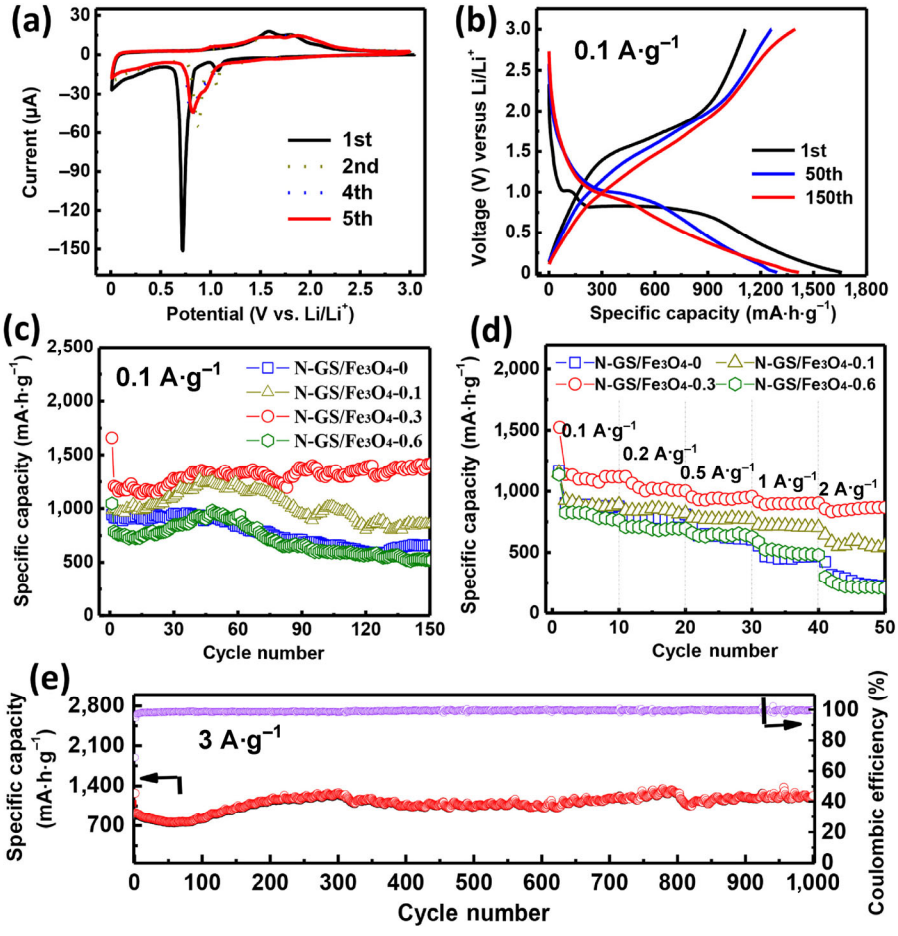


**Figure 4** (a) CV curves of N-GS/$Fe_3O_4$-0.3 obtained at a 0.01 mV·$s^{-1}$ scan rate. (b) Selected charge/discharge curves of N-GS/$Fe_3O_4$-0.3 at a current density of 100 mA·$g^{-1}$. (c) Cycling and (d) rate performance of N-GS/$Fe_3O_4$-0, N-GS/$Fe_3O_4$-0.1, N-GS/$Fe_3O_4$-0.3, and N-GS/$Fe_3O_4$-0.6. (e) Long-term cycling performance of N-GS/$Fe_3O_4$-0.3 at a current density of 3 A·$g^{-1}$.

increased with increased cycling. The initial discharge and charge capacities of the N-GS/$Fe_3O_4$-0.3 nanocomposite are 1,659 and 1,112 mA·h·$g^{-1}$, respectively. The first cycle Coulombic efficiency is ~67%. The large irreversible capacity of the first cycle is mainly attributed to the formation of a solid electrolyte interphase (SEI) layer on the electrode surface and irreversible Li insertion into the N-doped graphene matrix [59, 60].

N-GS has a specific capacity of ~1,177 mA·h·$g^{-1}$, as shown in the literature and our own experiment results [40]. The N-GS/$Fe_3O_4$-0.3 composite has ~73.5 wt.% of $Fe_3O_4$ and ~26.5 wt.% of N-GS according to the thermogravimetry analysis (TGA, Fig. S5 in the ESM). Theoretically, the specific capacity of the N-GS/$Fe_3O_4$-0.3 composite is ~993.9 mA·h·$g^{-1}$, that of $Fe_3O_4$ is ~682 mA·h·$g^{-1}$, and that of N-doped graphene is ~311.9 mA·h·$g^{-1}$. However, the first charge capacity at 0.1 A·$g^{-1}$ is ~1,100 mA·h·$g^{-1}$ based on the weight of N-GS/$Fe_3O_4$ composites, which is larger than the theoretical value. These phenomena have also been observed in many other reports [18, 31–32, 43]. Although it has been ascribed to the surface defects introduced by N-doping and side reactions of electrolyte degradation, clear understanding at the molecular level is needed, and further investigation is required using advanced characterization tools.

Figures 4(c) and 4(d) showed the cycling and rate performance of N-GS/$Fe_3O_4$-0.3 and control samples of N-GS/$Fe_3O_4$ nanocomposites obtained with different CTAB amounts. The N-GS/$Fe_3O_4$-0.3 sample obtained with the optimized CTAB amount shows the highest

specific capacity, the best cycling stability and rate performance. The specific capacity is ~1,200 mA·h·g$^{-1}$ at 0.1 A·g$^{-1}$, and its capacity fades very little over 150 cycles. The N-GS/$Fe_3O_4$-0.3 delivers a capacity of 867 mA·h·g$^{-1}$ at a high current density of 2 A·g$^{-1}$.

Long-term cycling stability at a high current density further corroborates the structural stability and rate performance of the sandwich structured nanocomposite. Figure 4(e) shows a typical cell with a capacity of ~1,000 mA·h·g$^{-1}$ and >90% retention over 1,000 cycles at 3 A·g$^{-1}$. The coulombic efficiency is 99.7% during stable cycling. Similar to many other graphene–metal-oxide composites [18, 23–26, 31, 32, 43], the capacity tends to increase with longer cycling, which is ascribed to the kinetically activated electrolyte degradation. Compared with the best result from recent studies on N-doped graphene/$Fe_3O_4$ and graphene/$Fe_3O_4$ electrodes (Tables S2 and S3 in the ESM), our sandwich structure nanocomposite shows a comparable specific capacity but a far superior high rate performance and cycle life.

The excellent electrochemical performance of our N-GS/$Fe_3O_4$ electrode can be ascribed to three aspects. 1) It exhibits a stable sandwich structure. The sandwich nanocomposite has very stable structure upon cycling. Figure S6 in the ESM shows the SEM images of the N-GS/$Fe_3O_4$-0.3 electrode after 1,000 cycles at 3 A·g$^{-1}$. It retained a sheet-like morphology covered with a thick layer of SEI film. 2) It exhibits small, uniform $Fe_3O_4$ particles uniformly distributed on the graphene sheets. Large-particle metal oxides exhibit poor reversibility and hence low specific capacity, poor cycling stability and rate performance. The N-GS/$Fe_3O_4$-0.3 obtained with the optimized CTAB amount has nearly monodisperse $Fe_3O_4$ nanoparticles of ~10 to 20 nm uniformly distributed on N-GS (Fig. 1). The control N-GS/$Fe_3O_4$ samples synthesized using too little or too much CTAB usually form large $Fe_3O_4$ particles or agglomerations (Fig. S1 in the ESM). The cycling stability and rate performance naturally are in descending order from N-GS/$Fe_3O_4$-0.3, to N-GS/$Fe_3O_4$-0.1, N-GS/$Fe_3O_4$-0.6, and N-GS/$Fe_3O_4$-0. 3) To verify the critical effect of N-doped graphene on the electrochemical performance, a control sample of graphene/$Fe_3O_4$ was prepared. The optimized amount of CTAB (~0.3 g) was used during the synthesis. The obtained sample also has nearly monodisperse $Fe_3O_4$ nanoparticles of ~10 to 20 nm (Fig. S7(a) in the ESM), and no significant agglomeration was observed. However, the electrochemical performance of the GS/$Fe_3O_4$-0.3 control sample tested using the same conditions as N-GS/$Fe_3O_4$-0.3 showed much poorer cycling stability and rate performance than N-GS/$Fe_3O_4$-0.3 (Figs. S7(b) and S7(c) in the ESM). The capacity retention is ~80% after 150 cycles at 0.1 A·g$^{-1}$, and the specific capacity is ~1,067 and 810 mA·h·g$^{-1}$ at 2 and 5 A·g$^{-1}$, respectively.

## 3 Conclusion

In summary, we prepared a sandwich-structured nanocomposite of N-GS and $Fe_3O_4$ by a self-assembly process under hydrothermal conditions. Through the interaction of N atoms with the graphene planes, surfactant molecules and iron precursors, iron oxide nanoparticles were well dispersed on N-doped graphene around N sites with a nearly monodisperse diameter of ~10 to 20 nm. N-doped graphene not only controls the nucleation of $Fe_3O_4$ but also works as the conducting framework in the nanocomposite. The unique structure enables good conductivity and Li-ion accessibility, can accommodate a large volume change, and hence exhibits good cycling reversibility and rate performance. A capacity of ~1,227 mA·h·g$^{-1}$ with 96.8% retention over 1,000 cycles was obtained at the current density of 3 A·g$^{-1}$. In terms of the facile method of graphene oxide reduction, N doping and N-controlled nucleation, and self-assembly of sandwich structures, our work provides good guidance in designing desirable structures for conversion anode materials or other electrode materials that undergo a large volume change.

## 4 Experimental section

### 4.1 Material synthesis

GO was prepared using a modified Hummers method [61]. In a typical synthesis, graphene oxide (~40 mg) was dispersed in a mixed solvent of ethylene glycol and deionized (DI) water (30 mL, volume ratio of 1:2) under sonication for 1 h to obtain a well-dispersed

GO suspension. Subsequently, CTAB (~0.3 g) was added under vigorous stirring to achieve a uniform dispersion. After iron acetylacetonate (~0.353 g) was added into the mixture, an ammonia solution (~10 mL, 25 wt.%–28 wt.%) and hydrazine hydrate (~10 mL) were added separately into the mixture under vigorous stirring for 30 min to obtain a dark, homogeneous solution. The solution was transferred into a 100 mL Teflon-lined stainless steel autoclave and heated at 180 °C for 16 h. The final product was collected by centrifugation, washed sequentially with ethanol and deionized water, and then dried at 80 °C overnight. Samples with different amounts of CTAB ranging from 0 to 0.6 g were prepared by a similar procedure. The products are denoted as N-GS/$Fe_3O_4$-0, N-GS/$Fe_3O_4$-0.1, N-GS/$Fe_3O_4$-0.3 and N-GS/$Fe_3O_4$-0.6.

A control sample of graphene/iron oxide with 0.3 g CTAB (denoted as GS/$Fe_3O_4$-0.3) was prepared using a similar procedure [62]. N-GS was also produced using a similar procedure but without iron acetylacetonate and CTAB.

### 4.2 Characterization

The morphology and structure of the samples were characterized using SEM (FEI Nano450). TEM, HRTEM, selected-area electron diffraction (SAED), and EDS mapping were carried out on a Tecnai G2 F20 operated at 200 kV. The phase purity and crystal structure of the samples were examined by XRD (Bruker D8) with Cu K$\alpha$ radiation at 40 kV and 40 mA from 8° to 90°. Raman measurements were carried out on a HORIBA JOBIN YVON S.A.S. system (model LabRAM HR800) with a 532 nm laser. The XPS data was collected with an ESCALab220i-XL electron spectrometer from VG Scientific using 300 W Al K radiation. The binding energies obtained in the XPS analysis were corrected with reference to C1s (284.8 eV). TGA was carried out with a NETZSCH STA 449C in the temperature range of 50–800 °C at a heating rate of 5 °C·min$^{-1}$ in air. Nitrogen sorption isotherms were obtained using a Quantachrome autosorb automated gas sorption system at –196 °C. Specific surface areas and pore size distributions were calculated using the BET theory and the Barrett–Joyner–Halenda (BJH) method, respectively, based on the desorption branches. Specific pore volumes were measured at a relative pressure of 0.99.

### 4.3 Computation

Periodic self-consistent DFT calculations were performed with the CASTEP module [63] in Materials Studio 6.1 to unravel the preferential bonding between iron oxide and different substrates. The model adsorption systems were described as an optimized $Fe_3O_4$ cluster that was cut from an $Fe_3O_4$ bulk cubic inverse spinel structure supported on the (6 × 6) supercell PG, NG, as well as the NVG. The projector-augmented-wave (PAW) method, combined with a planewave cut-off energy of 300 eV was used to describe the core and valence electrons [64]. The Perdew–Burke–Ernzerhof (PBE) form of the generalized gradient approximation (GGA) [65] was implemented in all of the calculations. For more details, please see the ESM.

### 4.4 Electrochemical measurements

The N-GS/$Fe_3O_4$ sample was mixed with carbon black and polyvinylidene fluoride (80:10:10 by weight ratio) in N-methyl-2-pyrrolidone to form a slurry, which was then coated on copper foil. The electrodes were dried in a vacuum oven for 24 h, weighed, and moved into the glovebox. The mass loading of the active material was ~1 mg·cm$^{-2}$. The electrochemical performance was tested using 2025-type coin cells. Li metal foil was used as the counter electrode. The electrolyte was 1 M $LiPF_6$ in a mixture of ethylene carbonate (EC), diethyl carbonate (DMC) and fluoroethylene carbonate (EMC) (1:1:1 by volume), and Celgard 2400 was used as the separator. The coin cells were assembled in an argon-filled glove-box (Braun, Germany). Galvanostatic charge/discharge tests were carried out on a Land battery test system (Land BT2001A, Wuhan, China) between 0.01 and 3.0 V versus Li/Li$^+$. CV was performed at a scan rate of 0.01 mV·s$^{-1}$ within the range of 0.01–3.0 V on an electrochemical workstation (VMP3, Bio-Logic SA, France).

## Acknowledgements

The authors would like to acknowledge financial supports from the National High-tech R&D Program of China (863 Program) (Nos. 2013AA032002 and 2015AA034601), China Iron & Steel Research Institute

Group Foundation (No. SHI11AT0540A) and Advance Technology & Materials Co., Ltd Innovation Foundations (No. 2013JA02PYF).

**Electronic Supplementary Material**: Supplementary material (SEM imaging, XPS, TGA curves, and DFT calculation) is available in the online version of this article at https://doi.org/10.1007/s12274-017-1502-x.

## References


[1] Poizot, P.; Laruelle, S.; Grugeon, S.; Dupont, L.; Tarascon, J. M. Nano-sized transition-metal oxides as negative-electrode materials for lithium-ion batteries. *Nature* **2000**, *407*, 496–499.

[2] Croguennec, L.; Palacin, M. R. Recent achievements on inorganic electrode materials for lithium-ion batteries. *J. Am. Chem. Soc.* **2015**, *137*, 3140–3156.

[3] Wang, H. L.; Dai, H. J. Strongly coupled inorganic–nano-carbon hybrid materials for energy storage. *Chem. Soc. Rev.* **2013**, *42*, 3088–3113.

[4] Pop, E. Energy dissipation and transport in nanoscale devices. *Nano Res.* **2010**, *3*, 147–169.

[5] Tarascon, J. M.; Armand, M. Issues and challenges facing rechargeable lithium batteries. *Nature* **2001**, *414*, 359–367.

[6] Reddy, M. V.; Subba Rao, G. V.; Chowdari, B. V. R. Metal oxides and oxysalts as anode materials for Li ion batteries. *Chem. Rev.* **2013**, *113*, 5364–5457.

[7] Tuček, J.; Kemp, K. C.; Kim, K. S.; Zbořil, R. Iron-oxide-supported nanocarbon in lithium-ion batteries, medical, catalytic, and environmental applications. *ACS Nano* **2014**, *8*, 7571–7612.

[8] Zhang, H. W.; Zhou, L.; Noonan, O.; Martin, D. J.; Whittaker, A. K.; Yu, C. Z. Tailoring the void size of iron oxide@carbon yolk–shell structure for optimized lithium storage. *Adv. Funct. Mater.* **2014**, *24*, 4337–4342.

[9] Yang, Y. Q.; Zhang, J. N.; Wu, X. C.; Fu, Y. S.; Wu, H. X.; Guo, S. W. Composites of boron-doped carbon nanosheets and iron oxide nanoneedles: Fabrication and lithium ion storage performance. *J. Mater. Chem. A* **2014**, *2*, 9111–9117.

[10] Ban, C. M.; Wu, Z. C.; Gillaspie, D. T.; Chen, L.; Yan, Y. F.; Blackburn, J. L.; Dillon, A. C. Nanostructured $Fe_3O_4$/SWNT electrode: Binder-free and high-rate Li-ion anode. *Adv. Mater.* **2010**, *22*, E145–E149.

[11] Jia, X. L.; Cheng, Y. H.; Lu, Y. F.; Wei, F. Building robust carbon nanotube-interweaved-nanocrystal architecture for high-performance anode materials. *ACS Nano* **2014**, *8*, 9265–9273.

[12] Chen, S. Q.; Bao, P. T.; Wang, G. X. Synthesis of $Fe_2O_3$–CNT–graphene hybrid materials with an open three-dimensional nanostructure for high capacity lithium storage. *Nano Energy* **2013**, *2*, 425–434.

[13] Chen, M. H.; Liu, J. L.; Chao, D. L.; Wang, J.; Yin, J. H.; Lin, J. Y.; Fan, H. J.; Shen, Z. X. Porous α-$Fe_2O_3$ nanorods supported on carbon nanotubes-graphene foam as superior anode for lithium ion batteries. *Nano Energy* **2014**, *9*, 364–372.

[14] Sun, Z. Y.; Xie, K. P.; Li, Z. A.; Sinev, I.; Ebbinghaus, P.; Erbe, A.; Farle, M.; Schuhmann, W.; Muhler, M.; Ventosa, E. Hollow and yolk-shell iron oxide nanostructures on few-layer graphene in Li-ion batteries. *Chem.—Eur. J.* **2014**, *20*, 2022–2030.

[15] Hu, J. T.; Zheng, J. X.; Tian, L. L.; Duan, Y. D.; Lin, L. P.; Cui, S. H.; Peng, H.; Liu, T. C.; Guo, H.; Wang, X. W. et al. A core–shell nanohollow-γ-$Fe_2O_3$@graphene hybrid prepared through the kirkendall process as a high performance anode material for lithium ion batteries. *Chem. Commun.* **2015**, *51*, 7855–7858.

[16] An, Q. Y.; Lv, F.; Liu, Q. Q.; Han, C. H.; Zhao, K. N.; Sheng, J. Z.; Wei, Q. L.; Yan, M. Y.; Mai, L. Q. Amorphous vanadium oxide matrixes supporting hierarchical porous $Fe_3O_4$/graphene nanowires as a high-rate lithium storage anode. *Nano Lett.* **2014**, *14*, 6250–6256.

[17] Luo, J. S.; Liu, J. L.; Zeng, Z. Y.; Ng, C. F.; Ma, L. J.; Zhang, H.; Lin, J. Y.; Shen, Z. X.; Fan, H. J. Three-dimensional graphene foam supported $Fe_3O_4$ lithium battery anodes with long cycle life and high rate capability. *Nano Lett.* **2013**, *13*, 6136–6143.

[18] Wei, W.; Yang, S. B.; Zhou, H. X.; Lieberwirth, I.; Feng, X. L.; Müllen, K. 3d graphene foams cross-linked with pre-encapsulated $Fe_3O_4$ nanospheres for enhanced lithium storage. *Adv. Mater.* **2013**, *25*, 2909–2914.

[19] Yu, S. H.; Conte, D. E.; Baek, S.; Lee, D. C.; Park, S. K.; Lee, K. J.; Piao, Y. Z.; Sung, Y. E.; Pinna, N. Structure-properties relationship in iron oxide-reduced graphene oxide nanostructures for Li-ion batteries. *Adv. Funct. Mater.* **2013**, *23*, 4293–4305.

[20] Wang, H. W.; Xu, Z. J.; Yi, H.; Wei, H. G.; Guo, Z. H.; Wang, X. F. One-step preparation of single-crystalline $Fe_2O_3$ particles/graphene composite hydrogels as high performance anode materials for supercapacitors. *Nano Energy* **2014**, *7*, 86–96.

[21] Zhao, B. T.; Zheng, Y.; Ye, F.; Deng, X.; Xu, X. M.; Liu, M. L.; Shao, Z. P. Multifunctional iron oxide nanoflake/graphene composites derived from mechanochemical synthesis for enhanced lithium storage and electrocatalysis. *ACS Appl. Mater. Interfaces* **2015**, *7*, 14446–14455.

[22] Lee, K. S.; Park, S.; Lee, W.; Yoon, Y. S. Hollow nanobarrels

of α-$Fe_2O_3$ on reduced graphene oxide as high-performance anode for lithium-ion batteries. *ACS Appl. Mater. Interfaces* **2016**, *8*, 2027–2034.

[23] Pan, L.; Zhu, X. D.; Xie, X. M.; Liu, Y. T. Smart hybridization of $TiO_2$ nanorods and $Fe_3O_4$ nanoparticles with pristine graphene nanosheets: Hierarchically nanoengineered ternary heterostructures for high-rate lithium storage. *Adv. Funct. Mater.* **2015**, *25*, 3341–3350.

[24] Li, Q.; Mahmood, N.; Zhu, J. H.; Hou, Y. L.; Sun, S. H. Graphene and its composites with nanoparticles for electrochemical energy applications. *Nano Today* **2014**, *9*, 668–683.

[25] Wang, Z. Y.; Liu, C. J. Preparation and application of iron oxide/graphene based composites for electrochemical energy storage and energy conversion devices: Current status and perspective. *Nano Energy* **2015**, *11*, 277–293.

[26] Wu, S. P.; Xu, R.; Lu, M. J.; Ge, R. Y.; Iocozzia, J.; Han, C. P.; Jiang, B. B.; Lin, Z. Q. Graphene-containing nanomaterials for lithium-ion batteries. *Adv. Energy Mater.* **2015**, *5*, 1500400.

[27] Fei, H. L.; Peng, Z. W.; Li, L.; Yang, Y.; Lu, W.; Samuel, E. L. G.; Fan, X. J.; Tour, J. M. Preparation of carbon-coated iron oxide nanoparticles dispersed on graphene sheets and applications as advanced anode materials for lithium-ion batteries. *Nano Res.* **2014**, *7*, 502–510.

[28] Li, L.; Gao, C. T.; Kovalchuk, A.; Peng, Z. W.; Ruan, G. D.; Yang, Y.; Fei, H. L.; Zhong, Q. F.; Li, Y. L.; Tour, J. M. Sandwich structured graphene-wrapped FeS-graphene nanoribbons with improved cycling stability for lithium ion batteries. *Nano Res.* **2016**, *9*, 2904–2911.

[29] Wang, D. H.; Kou, R.; Choi, D.; Yang, Z. G.; Nie, Z. M.; Li, J.; Saraf, L. V.; Hu, D. H.; Zhang, J. G.; Graff, G. L. et al. Ternary self-assembly of ordered metal oxide–graphene nanocomposites for electrochemical energy storage. *ACS Nano* **2010**, *4*, 1587–1595.

[30] Li, X. L.; Qi, W.; Mei, D. H.; Sushko, M. L.; Aksay, I.; Liu, J. Functionalized graphene sheets as molecular templates for controlled nucleation and self-assembly of metal oxide-graphene nanocomposites. *Adv. Mater.* **2012**, *24*, 5136–5141.

[31] Wood, K. N.; O'Hayre, R.; Pylypenko, S. Recent progress on nitrogen/carbon structures designed for use in energy and sustainability applications. *Energy Environ. Sci.* **2014**, *7*, 1212–1249.

[32] Liu, S. H.; Dong, Y. F.; Zhao, C. T.; Zhao, Z. B.; Yu, C.; Wang, Z. Y.; Qiu, J. S. Nitrogen-rich carbon coupled multifunctional metal oxide/graphene nanohybrids for long-life lithium storage and efficient oxygen reduction. *Nano Energy* **2015**, *12*, 578–587.

[33] Wang, X. W.; Sun, G. Z.; Routh, P.; Kim, D. H.; Huang, W.; Chen, P. Heteroatom-doped graphene materials: Syntheses, properties and applications. *Chem. Soc. Rev.* **2014**, *43*, 7067–7098.

[34] Wang, X.; Cao, X. Q.; Bourgeois, L.; Guan, H.; Chen, S. M.; Zhong, Y. T.; Tang, D. M.; Li, H. Q.; Zhai, T. Y.; Li, L. et al. N-doped graphene-$SnO_2$ sandwich paper for high-performance lithium-ion batteries. *Adv. Funct. Mater.* **2012**, *22*, 2682–2690.

[35] Song, J. X.; Xu, T.; Gordin, M. L.; Zhu, P. Y.; Lv, D. P.; Jiang, Y. B.; Chen, Y. S.; Duan, Y. H.; Wang, D. H. Nitrogen-doped mesoporous carbon promoted chemical adsorption of sulfur and fabrication of high-areal-capacity sulfur cathode with exceptional cycling stability for lithium-sulfur batteries. *Adv. Funct. Mater.* **2014**, *24*, 1243–1250.

[36] Li, X. L.; Wang, H. L.; Robinson, J. T.; Sanchez, H.; Diankov, G.; Dai, H. J. Simultaneous nitrogen doping and reduction of graphene oxide. *J. Am. Chem. Soc.* **2009**, *131*, 15939–15944.

[37] Qu, L. T.; Liu, Y.; Baek, J. B.; Dai, L. M. Nitrogen-doped graphene as efficient metal-free electrocatalyst for oxygen reduction in fuel cells. *ACS Nano* **2010**, *4*, 1321–1326.

[38] Marsden, A. J.; Brommer, P.; Mudd, J. J.; Dyson, M. A.; Cook, R.; Asensio, M.; Avila, J.; Levy, A.; Sloan, J.; Quigley, D. et al. Effect of oxygen and nitrogen functionalization on the physical and electronic structure of graphene. *Nano Res.* **2015**, *8*, 2620–2635.

[39] Wu, Z. S.; Ren, W. C.; Xu, L.; Li, F.; Cheng, H. M. Doped graphene sheets as anode materials with superhigh rate and large capacity for lithium ion batteries. *ACS Nano* **2011**, *5*, 5463–5471.

[40] He, C. Y.; Wang, R. H.; Fu, H. G.; Shen, P. K. Nitrogen-self-doped graphene as a high capacity anode material for lithium-ion batteries. *J. Mater. Chem.* **2013**, *1*, 14586–14591.

[41] Chang, Y. H.; Li, J.; Wang, B.; Luo, H.; He, H. Y.; Song, Q.; Zhi, L. J. Synthesis of 3d nitrogen-doped graphene/$Fe_3O_4$ by a metal ion induced self-assembly process for high-performance li-ion batteries. *J. Mater. Chem.* **2013**, *1*, 14658–14665.

[42] Yang, L.; Guo, G. N.; Sun, H. J.; Shen, X. D.; Hu, J. H.; Dong, A. G.; Yang, D. Ionic liquid as the C and N sources to prepare yolk–shell $Fe_3O_4$@N-doped carbon nanoparticles and its high performance in lithium-ion battery. *Electrochim. Acta* **2016**, *190*, 797–803.

[43] Zhou, X. S.; Wan, L. J.; Guo, Y. G. Binding $SnO_2$ nanocrystals in nitrogen-doped graphene sheets as anode materials for lithium-ion batteries. *Adv. Mater.* **2013**, *25*, 2152–2157.

[44] Qiu, Y. C.; Li, W. F.; Zhao, W.; Li, G. Z.; Hou, Y.; Liu, M. N.; Zhou, L. S.; Ye, F. M.; Li, H. F.; Wei, Z. H. et al. High-rate, ultralong cycle-life lithium/sulfur batteries enabled by nitrogen-doped graphene. *Nano Lett.* **2014**, *14*, 4821–4827.

[45] Yun, S.; Lee, Y. C.; Park, H. S. Phase-controlled iron oxide nanobox deposited on hierarchically structured graphene networks for lithium ion storage and photocatalysis. *Sci. Rep.* **2016**, *6*, 19959.

[46] Yu, X. B.; Qu, B.; Zhao, Y.; Li, C. Y.; Chen, Y. J.; Sun, C. W.; Gao, P.; Zhu, C. L. Growth of hollow transition metal (Fe, Co, Ni) oxide nanoparticles on graphene sheets through kirkendall effect as anodes for high-performance lithium-ion batteries. *Chem.—Eur. J.* **2016**, *22*, 1638–1645.

[47] Zhang, Z. H.; Wang, F.; An, Q.; Li, W.; Wu, P. Y. Synthesis of graphene@ $Fe_3O_4$@C core–shell nanosheets for high-performance lithium ion batteries. *J. Mater. Chem.* **2015**, *3*, 7036–7043.

[48] Zhang, L.; Wu, H. B.; Lou, X. W. Iron-oxide-based advanced anode materials for lithium-ion batteries. *Adv. Energy Mater.* **2014**, *4*, 1300958.

[49] Han, F.; Ma, L. J.; Sun, Q.; Lei, C.; Lu, A. H. Rationally designed carbon-coated $Fe_3O_4$ coaxial nanotubes with hierarchical porosity as high-rate anodes for lithium ion batteries. *Nano Res.* **2014**, *7*, 1706–1717.

[50] Liu, Y. P.; Huang, K.; Luo, H.; Li, H. X.; Qi, X.; Zhong, J. X. Nitrogen-doped graphene-$Fe_3O_4$ architecture as anode material for improved Li-ion storage. *RSC Adv.* **2014**, *4*, 17653–17659.

[51] Qin, G. H.; Fang, Z. W.; Wang, C. Y. Template free construction of a hollow $Fe_3O_4$ architecture embedded in an N-doped graphene matrix for lithium storage. *Dalton Trans.* **2015**, *44*, 5735–5745.

[52] Lu, X. Y.; Wang, R. H.; Bai, Y.; Chen, J. J.; Sun, J. Facile preparation of a three-dimensional $Fe_3O_4$/macroporous graphene composite for high-performance li storage. *J. Mater. Chem.* **2015**, *3*, 12031–12037.

[53] Sakthivel, T.; Gunasekaran, V.; Kim, S. J. Effect of oxygenated functional groups on the photoluminescence properties of graphene-oxide nanosheets. *Mater. Sci. Semicond. Process.* **2014**, *19*, 174–178.

[54] Tang, L. H.; Wang, Y.; Li, Y. M.; Feng, H. B.; Lu, J.; Li, J. H. Preparation, structure, and electrochemical properties of reduced graphene sheet films. *Adv. Funct. Mater.* **2009**, *19*, 2782–2789.

[55] Sun, L.; Wang, L.; Tian, C. G.; Tan, T. X.; Xie, Y.; Shi, K. Y.; Li, M. T.; Fu, H. G. Nitrogen-doped graphene with high nitrogen level via a one-step hydrothermal reaction of graphene oxide with urea for superior capacitive energy storage. *RSC Adv.* **2012**, *2*, 4498–4506.

[56] Chen, P.; Xiao, T. Y.; Qian, Y. H.; Li, S. S.; Yu, S. H. A nitrogen-doped graphene/carbon nanotube nanocomposite with synergistically enhanced electrochemical activity. *Adv. Mater.* **2013**, *25*, 3192–3196.

[57] Li, L.; Kovalchuk, A.; Fei, H. L.; Peng, Z. W.; Li, Y. L.; Kim, N. D.; Xiang, C. S.; Yang, Y.; Ruan, G. D.; Tour, J. M. Enhanced cycling stability of lithium-ion batteries using graphene-wrapped $Fe_3O_4$-graphene nanoribbons as anode materials. *Adv. Energy Mater.* **2015**, *5*, 1500171.

[58] Jiang, X.; Yang, X. L.; Zhu, Y. H.; Yao, Y. F.; Zhao, P.; Li, C. Z. Graphene/carbon-coated $Fe_3O_4$ nanoparticle hybrids for enhanced lithium storage. *J. Mater. Chem.* **2015**, *3*, 2361–2369.

[59] Yang, S. B.; Sun, Y.; Chen, L.; Hernandez, Y.; Feng, X. L.; Müllen, K. Porous iron oxide ribbons grown on graphene for high-performance lithium storage. *Sci. Rep.* **2012**, *2*, 427.

[60] Zhou, G. M.; Wang, D. W.; Li, F.; Zhang, L. L.; Li, N.; Wu, Z. S.; Wen, L.; Lu, G. Q.; Cheng, H. M. Graphene-wrapped $Fe_3O_4$ anode material with improved reversible capacity and cyclic stability for lithium ion batteries. *Chem. Mater.* **2010**, *22*, 5306–5313.

[61] McAllister, M. J.; Li, J. L.; Adamson, D. H.; Schniepp, H. C.; Abdala, A. A.; Liu, J.; Herrera-Alonso, M.; Milius, D. L.; Car, R.; Prud'homme, R. K. et al. Single sheet functionalized graphene by oxidation and thermal expansion of graphite. *Chem. Mater.* **2007**, *19*, 4396–4404.

[62] Su, J.; Cao, M. H.; Ren, L.; Hu, C. W. $Fe_3O_4$–graphene nanocomposites with improved lithium storage and magnetism properties. *J. Phys. Chem. C* **2011**, *115*, 14469–14477.

[63] Segall, M. D.; Philip, J. D. L.; Probert, M. J.; Pickard, C. J.; Hasnip, P. J.; Clark, S. J.; Payne, M. C. First-principles simulation: Ideas, illustrations and the CASTEP code. *J. Phys.: Condens. Matter* **2002**, *14*, 2717–2744.

[64] Perdew, J. P.; Burke, K.; Ernzerhof, M. Generalized gradient approximation made simple. *Phys. Rev. Lett.* **1996**, *77*, 3865–3868.

[65] Kresse, G.; Joubert, D. From ultrasoft pseudopotentials to the projector augmented-wave method. *Phys. Rev. B* **1999**, *59*, 1758–1775.